IEEE Access
Multidisciplinary | Rapid Review | Open Access Journal

SPECIAL SECTION ON MISSION CRITICAL SENSORS AND SENSOR NETWORKS (MC-SSN)

Received February 12, 2019, accepted February 20, 2019, date of publication March 18, 2019, date of current version April 9, 2019.

Digital Object Identifier 10.1109/ACCESS.2019.2905600

A Partial-Dip Observation Mechanism for the Resolution Improvement of Spectrum-Like Surface Plasmon Resonance Waveforms

CHENG WANG

Department of Artificial Intelligence, College of Electronic and Communication Engineering, Tianjin Normal University, Tianjin 300387, China
Tianjin Key Laboratory of Wireless Mobile Communications and Power Transmission, Tianjin Normal University, Tianjin 300387, China

e-mail: cwang@tjnu.edu.cn

This work was supported by the Science and Technology Development Fund of Tianjin Education Commission for Higher Education under Grant 2018KJ153.

ABSTRACT Continuum of signals exhibiting spectral features, such as asymmetric waveforms and peaks, are common in optoelectric measurements. In ordinary circumstances, the peaks of spectrum-like waveforms carry critical information, and accurately identifying peak location is of great significance. However, due to the finite hardware resources of practical electrical instruments, the accuracy of peak identifying is usually limited. To improve the resolution performance without hardware upgrading, we propose a weighted centroid algorithm in this paper. Based on a representative experimental verification of surface plasmon resonance sensor system under angular-interrogation, we propose that the peak-locating performance is primarily determined by the dramatically changing part, rather than the entire waveform. By manually cutting out the partial waveform with drastic change ratio via an appropriate gain amplification, the accuracy of spectrum-like signal locating is capable to be enhanced, and the sensor resolution performance, nearly one order of magnitude.

INDEX TERMS Spectrum-like waveform, peak locating accuracy, surface plasmon resonance, partial-dip observation, twice weighted centroid algorithm.

I. INTRODUCTION

Surface plasmon resonance (SPR) sensors are commonly used as a refractive index (RI) measurement tool of liquid samples because of the highly sensitive and real-time advantages [1], [2]. SPR sensors employ several modes [3]–[6], in which the type employs angular-interrogation is the most popular one [7] because of the simple fabrication, maturity and reliability. Based on the angular-interrogation, SPR phenomena arising from RI changes of the liquid sample can be detected by monitoring an attenuated total reflection (ATR) intensity curves. Typical ATR responses are spectrum-like waveforms of reflective intensity versus incident angle. The incident angle values can be determined by discrete pixels which linear arranged on the photo-detector, corresponding reflective intensity values can be observed by an analog-to-digital converter (ADC). As shown in Figure 1, on the ATR curve, the most evident identifier is the minimum intensity point, the corresponding angle value is named resonance angle (RA). In practical applications, special algorithms are usually employed to extract information of ATR shifts as the responses rather than directly observe the RA values. Thereby, the SPR responses can identify weak shifts, which are smaller than the angle covered by a single pixel.

For higher performances, researchers have proposed a numbers of observation mechanisms and algorithms [8]. Summarizing these works, all their observation targets were focused on the ATR curves [9]. Hence, the typical monitoring image is a spectrum-like waveform. Based on these sensing mechanisms, several centroid algorithms have been reported for accurately recognizing shifts of dip centroid as the responses of SPR sensors. For instance, ordinary centroid algorithm [10], weighted centroid algorithm [11], local similarity matching algorithm [12] and fast centroid algorithm [13], all these algorithms provide strengths and advantages respectively. In this article, the author proposes a novel monitoring mechanism named ''partial-dip observation mechanism'', which discards the entire waveform and focus on a more identifiable partial part on the ATR curve.

The associate editor coordinating the review of this manuscript and approving it for publication was Qilian Liang.

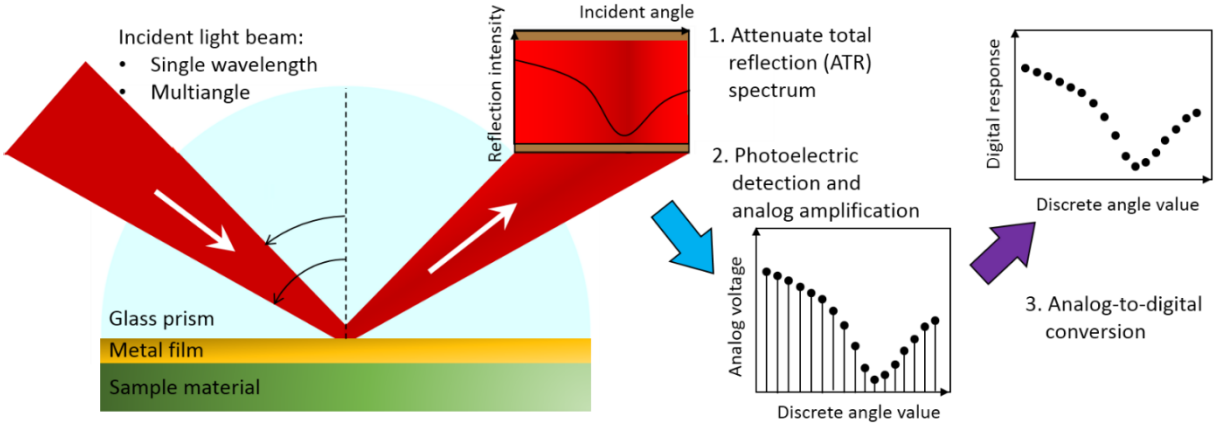

FIGURE 1. Measurement of spectrum-like waveforms generated by an angular-interrogation surface plasmon resonance setup. An attenuated total reflection spectrum is in order detected by a photodetector and analog-to-digital convertor with finite resolution.

The experiment results demonstrate that under the exactly same testing surrounding, the novel mechanism can significantly improve the identifying ability of weak RI changes, without any enhancement of sensor hardware update.

II. METHODS

A. PERFORMANCE PARAMETERS

There are two important parameters for SPR sensors, the sensitivity S and the resolution σ_{RI}. As defined [1], sensitivity is the ratio of the change in SPR sensor output to the change in the quantity to be measured (RI). It can be defined as the quotient of ATR curve shifts and RI changes:

$$S = S_1 \cdot S_2 = \frac{\delta R}{\delta n_{\text{ef}}} \cdot \frac{\delta n_{\text{ef}}}{\delta n} \tag{1}$$

In Eq. (1), R is sensor response. In this article, it is the centroid other than RA. The first term $S_1 = \delta R/\delta n_{\text{ef}}$ describes the response sensitivity to the effective index of a surface plasmon. The second term $S_2 = \delta n_{\text{ef}}/\delta n$ describes the sensitivity of the effective index to the RI value. Theoretically, S is not a constant. In RI detections, the second term S_2 is a continuously increasing function with the absolute value increment of RI [14]–[17]. If the RI variation range is not very broad, there is an approximate linear relationship between S_2 and the corresponding RI value. For a practical SPR sensor, S_2 is determined by its physical structure, such as material of substrate, metal film, wavelength of the light source and exploitation method. For the first term S_1, it is a saw-toothed discontinuous function. Because of the finite pixels and ADC bits, both the continuously distributed incidental angle and corresponding intensity values are detected as discrete values. S_1 usually displays response lags, when the RI value is still within a sufficiently narrow interval, S_1 keeps unchanged [18]. This phenomenon is defined as the sensitivity deviation, although S_1 keeps an approximate linear tendency. And denser pixels, more ADC bits and proper algorithm used, better smoothness S_1 displays.

Another parameter is the limit of detection (LOD) of RI change magnitude [19] named the RI resolution σ_{RI}. Resolution defines the smallest change in the RI that produces a detectable change in the sensor output [1]. σ_{RI} is defined as:

$$\sigma_{\text{RI}} = \frac{\sigma_{\text{s}}}{S} \tag{2}$$

In Eq. (2), S is shown as Eq. (1), σ_{s} is the standard deviation of the sensor response which depends on the level of uncertainty of the sensor output (output noise level) [1]. Theoretically, σ_{s} is dependent on the performance of photo-detector, the bits of ADC and the numerical algorithm. Assuming that the noise level of the responses is below the digital error of the ADC, a perfect algorithm can identify an ATR shift with an error value equals $1/(2^n - 1)$ times the angle value covered by a single pixel [11]. Therefore, improving σ_{s} level is an effective route to make better σ_{RI} performance, which provides narrower confidence interval of RI measurement. On the other hand, suitable numerical algorithm reduces the deviation levels of S [20], which results in σ_{RI} fluctuations. In this work, the partial-dip sensing mechanism is utilized for lower σ_{s}, the twice weighted centroid algorithm can provide a more stable S. Thus, higher σ_{RI} could be realized.

B. APPARATUS

The sensor setup under the Kretschmann configuration (Figure 1) is built by the common commercial products as below.:

1) A 650 nm p-polarized laser beam was used as the exciting light source.
2) A BK7 glass prism ($n_p \approx 1.5145$) was used as the optical coupler, 5 nm Cr adhesive layer and 45nm Au film were deposited on it.
3) A photodiode array (Hamamatsu: S3903-1024Q) was used as the photo-detector. S3903 is a current output NMOS image sensor. The saturation charge of every pixel is 5 pC. In the setup, 1024 pixels cover an angle range $68 - 76°$. The mean of angle range $\Delta\alpha$ covered by a single pixel is $\sim 7.8 \times 10^{-3}$ °.

4) A current integration circuitry consisted of a switched integrator (Burr-Brown: IVC102) and a high performance amplifier (Burr-Brown: OPA404) were used as the drive circuit of S3903. The integration capacitance is 10 pF.
5) A 12 bits ADC (Maxim: MAX1315) for converting analog voltage signals into digital data.

And the theoretical performance of sensor setup is estimated based on performances of these components.

C. RESOLUTION ESTIMATION PRINCIPLE

Firstly, according to the Hamamatsu products handbook, S3903 keeps the root-mean-square (RMS) numbers of noise electrons less than 3000. So, the amount of noise charge is $\sim 3000 \times 1.6 \times 10^{-19} = 4.8 \times 10^{-16}$C. Comparing to its dynamic charge range (5 pC), S3903 should performs the output signal-noise-ratio (SNR) higher than 80 dB.

Secondly, the integrator IVC102 induces noises related to the integration capacitance and input capacitance. According to the handbook, when the integration capacitance was chosen 10 pF and the input capacitance from S3903 is about 30 pF, the RMS noise voltage is about 120 μV. Thus, consider that the output range is $5\text{pC}/10\text{pF} = 0.5\text{V}$, the SNR is about 72.4 dB. After the integrator, the amplifier OPA404 can provide accurate magnification with the SNR level over 100 dB, noises introduced is negligible.

Thirdly, the ADC MAX1315 has 1bit linear error, different form the RMS noise limited devices above, the discretization noise is peak-value limited. Corresponding SNR of ADC is around 72.2 dB.

According to the resolution theorems in [11], σ_s is approximately estimated to be lower than the level 1.9×10^{-6} °:

$$\sigma_s \leq 8 \times \frac{1}{1024} \times \frac{1}{4095} \approx 1.9 \times 10^{-6} \tag{3}$$

Consider that at room temperature, the sensitivity S of gold-water interface is $\sim 120°/\text{RIU}$ [21], the order of σ_{RI} should be $1.9 \times 10^{-6}/120 \approx 1.59 \times 10^{-8}$RIU. This is the theoretical limit of RI resolution under the ideal testing environment.

Moreover, the temperature fluctuations have to be considered as a major influence, due to the effective RI changes of liquid samples [21]. For SPR sensors used in biological or chemical analysis, liquid samples are usually dilute aqueous solution or hydrogel, temperature-dependent RI changes can be assumed as what of water. Based on previous researches, within a peak-to-peak inaccuracy 0.01° range, the RI maximum fluctuation is lower than 10^{-6}RIU [22]. Correspondingly, the standard deviation is $10^{-6}/6 \approx 1.67 \times 10^{-7}$RIU. Altogether these results suggest a upper limit at the order 1.59×10^{-8}RIU. And the angular-interrogation setup may not able to perform σ_{RI} level better than 1.67×10^{-7}RIU. On this occasion, the mission is improving σ_{RI} to the level nearly 1.67×10^{-7}RIU.

D. EXPERIMENTAL

Consider that liquid samples are usually dilute aqueous solutions. Water solutions with a little volume of ethanol can be used for simulating a kinetic process of RI increment. The monitoring target of SPR phenomena is the entire waveform under a priori baseline, which matches the ADC dynamic range. SPR responses (centroids) are calculated by using the centroid algorithm [11]:

$$centroid \overset{\text{def}}{=} \frac{\sum_{i=0}^{1023} \omega_i \left[R\left(X_i\right) - L\right] X_i}{\sum_{i=0}^{1023} \omega_i \left[R\left(X_i\right) - L\right]} \tag{4}$$

In Eq. (4), X_i is the pixel number, $R(X_i)$ is the corresponding intensity of X_i, L is the intensity baseline and $\omega_i = R(X_i) - L$ is the weight factor. The centroid given by Eq. (4) is a non-dimension value, an angular response can be done through a linear transform: $response = centroid \cdot \Delta\alpha$. Here $\Delta\alpha$ is the angle range covered by a single pixel. Different with the original centroid algorithm [10], the weighted centroid algorithm considered the pixel intensities nearby the baseline contribute smaller to the response, and weights each pixel a value ω_i to improve the response linearity [11].

Then, there are two parts in the experimental testing as follow:

A. Test responses of ethanol-water samples, in which ethanol content keeps a continuously increment from 0 to 2 mL. The liquid samples are prepared by absolute ethanol (2 mL total) and pure water (1 L). A peristaltic pump continuously injects 10 μL ethanol into the solution container per time, thus continuously increases the RI of the solution. The interval between every two injections is 2 minutes for a good mixing. According to previous researches [23]–[25], the RI change arising from ethanol ratio increase obey a proportional relationship in low concentration range. By converting volume ratio 2 ‰ into mass concentration ~ 1.58‰, the RI change per 0.0001RIU is corresponding to that adding 2 mL ethanol into 1 L water.
The ethanol solution driven by a peristaltic pump uniformly flows over the gold-water interface all the time. After each injection, the SPR sensor readily detects. An entire experimental process includes 200 responses. The test time length of a response is about 65.536 ms. In this way, the evolution process of SPR phenomena arising from RI changes can be acquired.
B. Test 6 ethanol solutions include specific volume of ethanol. The samples are prepared by mixing 0, 400, 800, 1200, 1600, 2000 μL ethanol into 1 L pure water, respectively. For 6 ethanol solutions, the detection of each solution are repeated 100 times. Intervals between every two data collections are about 500ms. Based on 600 SPR response results. Thus, the resolution σ_s level at 6 specific discrete ethanol contents can be acquired.

Figure 2 shows the results of the experiment part A. With respect to the RI increasing, the SPR responses show a rising but stepwise evolution indicating the sensitivity

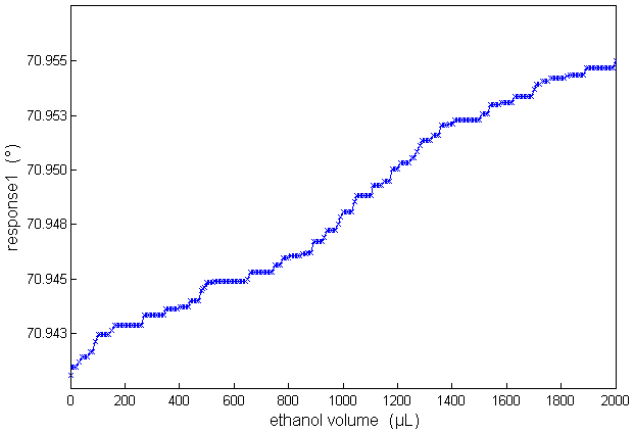

FIGURE 2. Sensor response evolution reflecting continuous RI increase of ethanol sample solution. The sensor responses are calculated based on the conventional entire-peak observation and regular centroid algorithm.

deviation [18]. Figure 3 shows the SPR responses of experiment part B, which clearly contain random noises.

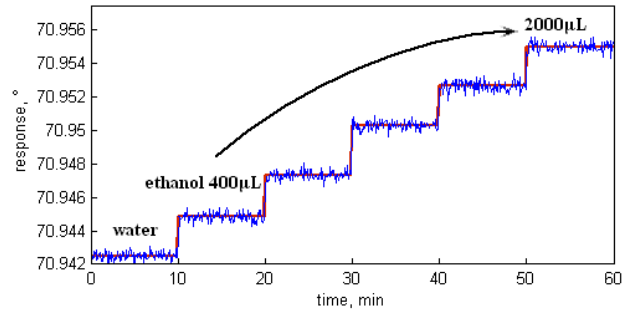

FIGURE 3. Sensor responses reproducibility characterized by ethanol samples with various RI values. The sensor responses are calculated based on the conventional entire-peak observation and regular centroid algorithm.

Furthermore, the statistics of the experimental results in Figure 3 are given in Table 1. Each mean or standard deviation corresponding to a specific ethanol volume was acquired from 100 continuously measurement responses. The standard deviation level could approximately replace the σ_s of SPR sensor for further discussion. As shown in Table 1, the average standard deviation level is $\sim 2.66 \times 10^{-4}$ °. And the sensitivity value $S \approx 120°/\text{RIU}$ [21] will be exploited to estimate the RI resolution σ_{RI}. As σ_{RI} maintains the order $\sim 2.66 \times 10^{-4}/120 \approx 2.2 \times 10^{-6}$RIU, the experimental sensor performance is much lower than the technical expectation level 1.67×10^{-7}RIU.

TABLE 1. Statistics of responses under conventional mechanism.

Ethanol content (μL)	Average of response (°)	Standard deviation of response (10^{-4} °)
0	70.94250	2.67869
400	70.94488	2.67405
800	70.94734	2.65319
1200	70.95032	2.68711
1600	70.95270	2.66568
2000	70.95502	2.66099

TABLE 2. Statistics of dark outputs noise of photodiode S3903.

Dynamic range of 12 bits ADC (V)	Gain of amplifier drive circuit	Mean of dark output (V)	Standard deviation of dark output (mV)	SNR (dB)
0 - 2.5	5	0.11063	0.98807	52.5
	10	0.11099	0.99951	52.4
	20	0.11140	1.07099	51.8
	30	0.11235	1.18168	50.9

III. RESOLUTION IMPROVEMENT PRINCIPLE

A. NOISE LEVEL

Since the measured σ_{RI} level is significantly lower than the theoretical order, the actual noise level should be worse than the ADC error level. As shown in Table 2, the noise level, as well as the dark response level of the photo-detector S3903, is measured to be $\sim$ 52.5dB in standard deviation parameter.

To reduce the noise influences, the centroid algorithms have been employed. However, in a weak shift process of ATR, the pixels near the RA position or the total reflection areas can hardly show visible intensity changes. In other words, they given almost nothing contribution to the identification of ATR shifts. The identifying ability is mainly provided by the pixels with rapid intensity changes.

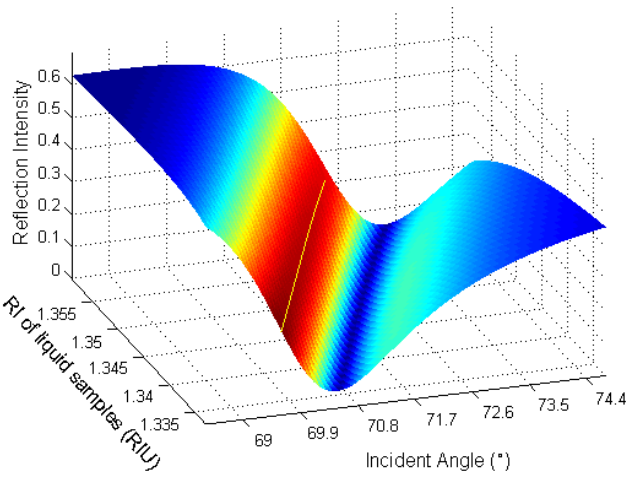

FIGURE 4. Theoretical evolution trend of ATR curve arising from RI increase. White line is the locus of most sensitive positions.

B. PARTIAL-DIP OBSERVATION

The model of angular-interrogation SPR sensors is built by Fresnel thin film equations. While the RI value is unchanged, there is a certainly constrained relationship between the light incident angle and corresponding reflection intensity. With respect to the RI value increasing, a continuous shift evolution of the ATR curve is shown as Figure 4, the dyeing colors show the intensity variation velocities on their own local position, from blue to red, the velocity gradually increases. In this way, if there is a more identifiable partial area existing on the waveform, in which the light intensity has faster change velocity versus the weak dip shift, the circuit gain can be increased to match the ADC dynamic range to this part of

the ATR dip. As a result, the identification ability of shifts will be improved. According to the data in Table 2, the SNR values remain on the level ∼ 50 dB. Therefore, the enhancement of useful information components and maintenance of noise components could make a noise decreasing effect in a disguised form. In this way, the SPR sensor could provide a considerable improvement of the RI resolution.

To get rid of complex iterations in Fresnel equations, the ATR curve as an asymmetric response function could be approximated as below [26]:

$$R(X) = A\left[1 - \frac{B + C(X - D)}{(X - D)^2 + E^2}\right] \tag{5}$$

In Eq. (5), X is the incident angle value. $R(X)$ is the intensity value correspond to X. A, B, C, D and E are all real parameters. They are associated with the physical structure of the SPR sensor. When the prism, metal film and light source are selected, the only factor can make them changing is the RI value n_s of the liquid sample. Another infinite series expression of Eq. (5) is shown as Eq. (6):

$$R(X) = \aleph_0(n_s) + \frac{\aleph_1(n_s)}{X} + \frac{\aleph_2(n_s)}{X^2} + \cdots = \sum_{n=0}^{+\infty} \frac{\aleph_n(n_s)}{X^n} \tag{6}$$

In Eq. (6), $R(X)$ is expressed as a convergent Laurent series form. Coefficients $\aleph_n$ in negative power terms are all real functions of n_s.

The realization of RI value changes depends on observing the pixels with an apparent shift of the ATR arising from a tiny RI change. For an unidentifiable sub-pixel shift, the intensity variation of pixels can provide a more accuracy auxiliary identifier. Hence, intensity values in somewhere with larger derivative values (absolute value) provide more obvious difference (as the colors shown in Figure 4). Based on Eq. (5), the first derivatives of $R(X)$ versus X is acquired (Figure 5b), which describes the intensity variation ratio with a weak dip shift. Previous researches have mentioned the maximum derivative point [27] and even pointed out the "inflection point" [28] provides the optimum observability. To indicate the orbit of the optimum points with the RI changes, the second order derivation of Eq. (5) is equaled to zero. The only real root $X = I$ is the inflection point, inflections always exist on the left side of ATR curves, $R(I)$ provides the highest identifiable response to sensing tiny shifts. The inflections orbit is shown as the white line in Figure 4 and their intensity values area is shown as the blue stripe in Figure 5a. The inflections are still within a stripe range much narrower than the full dynamic range.

Wider than the inflection area covering the orbit curve, the partial-dip monitoring area is shown as the lighter blue stripe in Figure 5a. Its intensity dynamic range matched by the ADC is at the middle of the full range, the amplitude width is about 1/5 of the former. As the near-red colors part shown in Figure 5a, by truncating the smooth parts which perform slow intensity variation ratio, the partial-dip area provides much more response information than conventional ATR dip does. In this case, the SNR of photo-detector still keeps on a 50 dB level, the partial-dip sensing could significantly improve the n_s performance.

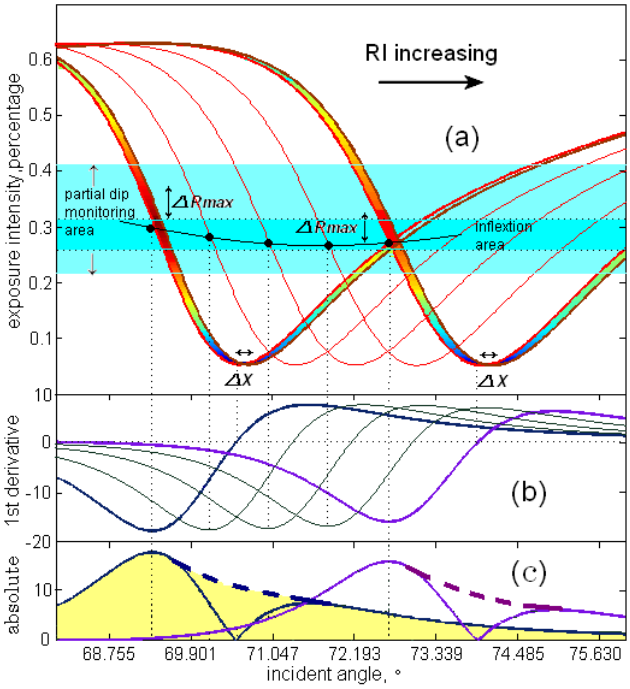

FIGURE 5. Inflections on ATR curves and the responses strength of tiny dip shifts. (a) Blue region is the intensity range which inflections distributed in, lighter blue region is the monitoring intensity range. (b) The inflection positions are located by the first derivatives. (c) The second weight factor functions (absolute value of the first derivative function) and their a fitting segment.

C. REVISED CENTROID ALGORITHM

As shown in Figure 6a, the entire ATR dip is replaced by an incomplete "partial-dip" in Figure 6b, tiny shifts of the graphs are more likely to be realized by observing 4 specific boundary pixels X_A, X_B, X_C and X_D. When the pixel number is smaller than X_A or bigger than X_D, its intensity value would be chopper rectified because of exceeding the ADC upper limit. By the same identifier, when pixel numbers are between X_B and X_C, intensities also would be rectified by the ADC lower limit. By using these 4 pixels, the range of the partial-dip can be determined to calculate the centroid.

Under the partial-dip sensing mechanism, the SNR level of photo-detector is higher than 50dB. When intensity signals are monitored by a 12 bits ADC, the width of intensity confidence interval could be calculated as: $W = 4095 \times 1/10^{\left(\frac{50}{20}\right)} \approx 12.95$. If a pixel which number is smaller than X_A, its intensity value should not be lower than the threshold: $4095 - W/2 \approx 4088$. When any pixel firstly performs an intensity value lower than 4088, it can be recognized as theX_A pixel in a probability higher than 99.5%. In the same way, the decision threshold of X_D is also 4088. For X_B and X_C, it is 7.

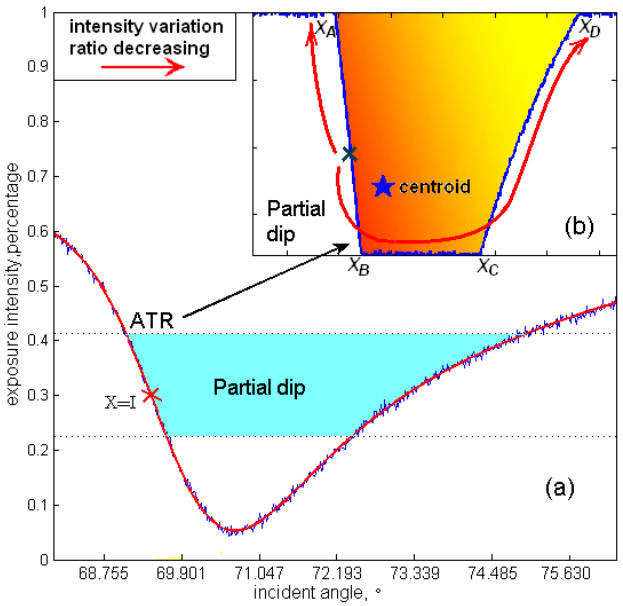

FIGURE 6. The partial-dip monitoring mechanism. (a) Entire waveform and monitoring area. (b) Partial-dip observation.

After the chosen of new monitoring target, a higher performance algorithm for partial-dip is also essential, because only the response surpassing the observation threshold is realizable. As a result, the SPR responses of a continuous RI increment usually show periodical saw-toothed details [18]. The intensity change of every pixel must be accumulated to a certain extent to induce a response change. According to Eq. (5) and Eq. (6), the intensity variation ratio which distributes on the partial-dip curve is not uniform. As red arrows shown in Figure 6b, from the inflection point $X = I$, the ratios of other points decrease along the directions of both sides. This means when a pixel locates on the rapid variation position, a weak shift can just make its intensity change visible, changes of other pixels absolutely can't be observed. In order to cope with this response lag effect and for a performing better linearity, a revised centroid algorithm named "twice weighted centroid" algorithm is proposed in this work, which employs an additional "intensity variation ratio weight" factor to compensate the nonlinearity of response. In that way, the pixel which is in the rapid variation position will contribute more information of centroid motions. This factor is approximately proportional to the intensity variation ratio or the absolute value of the first derivative of $R(X)$.

The first order derivation of Eq. (6), and also get a convergent Laurent series expression:

$$\frac{d\left[R\left(X\right)\right]}{dX} = \frac{\Psi_2\left(n_s\right)}{X^2} + \frac{\Psi_3\left(n_s\right)}{X^3} + \cdots = \sum_{n=2}^{+\infty} \frac{\Psi_n\left(n_s\right)}{X^n} \quad (7)$$

In Eq. (7), the power of the highest order term is -2. Figure 5b shows the function curves of Eq. (7), the intensity variation ratio curve has a maximum and a minimum. When the ATR dip moves to the right side, the intensity variation ratio curve synchronously moves right and becomes a little flatter.

Consider that the absolute value of Eq. (7) is not a continuous function nearby the RA point (as the solid curves shown in Figure 5c). The author try to define a smooth and continuous function for fitting the "intensity variation ratio weight" factor F_i (as the dash curves shown in Figure 5c), it can be expressed as Eq. (8):

$$F_i \overset{\text{def}}{=} \left| \frac{k}{\left(X_i - I\right)^2 I} \right| \quad (8)$$

In Eq. (8), k is the variation coefficient, which is a real constant determined by the noise level and the gain of photo-detector, X_i is the number of pixel, I is the number of the pixel which covered the inflection point. In this way, $(X_i - I)^2$ denotes the intensity variation ratio synchronously changes with the dip moving, it times I denotes the curve flatness changes with the position changes of dip. When the incident angle X is away from the discontinuity point, Eq. (8) can provide a perfect fitting approximation to the intensity variation ratio curve. But at the vicinity of the discontinuity point, errors are very serious. Fortunately, this situation is not a big deal, because under the partial-dip sensing mechanism, this "large error" part on the ART dip is already discarded. As shown in Figure 5a and 5c, the pixels correspond to the large error area are almost under the lower limit of ADC. In other words, their intensities are forcedly set zero. As the result, the values of their "intensity variation ratio weight" factors are very meaningless.

After the discussion of "intensity variation ratio weight" factor above, one last condition is yet to be fulfilled. The $X = I$ pixel of partial-dip has to be located to calculate the F_i factors. As the black curved orbit shown in Figure 5a, the intensity of inflections is still not a constant but a variable. Because of the chopper rectification of the entire ATR dip, the inflection position hardly can be acquired by using the global fitting method. Hence, the inflection pixel $X = I$ must be estimated only based on the partial-dip. As the green curve shown in Figure 7a, the intensities of the pixels between X_A and X_B are used to estimate the $X = I$ pixel. In this range, their first derivative curve performs a double-peak shape (Figure 7b). As zoomed in Figure 7c, the brown area under the zero baseline can be equaled into a centroid (black spots in Figure 7b and 7c). As the same view that centroid of ATR curve is an approximate representation of RA, this centroid of the first derivative curve is an estimate of the inflection pixel.

Based on the discussion above, an approximation of the inflection point $\tilde{I}$ can be estimated as Eq. (9). For some reasons which will be introduced later, this formula utilizes the original centroid algorithm [10], but the function $R(X)$ is replaced by the first derivative function $d\left[R\left(X\right)\right]/dX$.

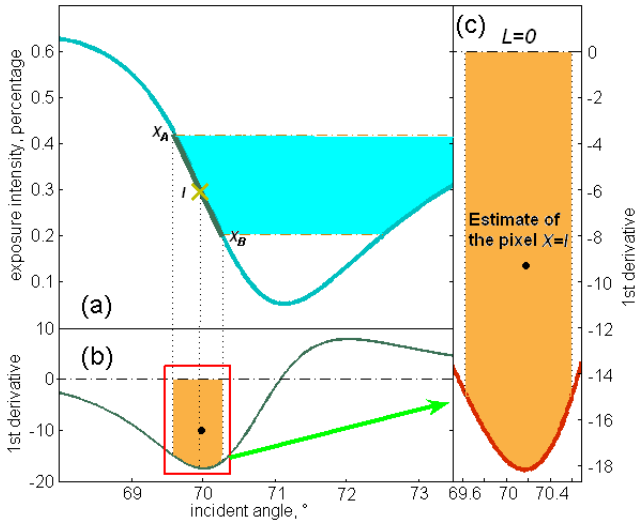

FIGURE 7. The estimation of inflection. (a) Pixels from X_A to X_B. (b) Corresponding derivative value range from X_A to X_B. (c) Derivative curve segment and its centroid, this centroid can been considered as an approximation of the inflection I.

The baseline constant L disappears, as it has been set to zero.

$$\tilde{I} \overset{\text{def}}{=} \frac{\sum_{i=A}^{B} X_i \left[\frac{d\,[R\,(X)]}{dX}\right]_{X=X_i}}{\sum_{i=A}^{B} \left[\frac{d\,[R\,(X)]}{dX}\right]_{X=X_i}} \tag{9}$$

In Eq. (9), $d\,[R\,(X)]/dX$ is unlikely to be calculated directly. But because of the particularities of Eq. (9), its result can be solved via other methods.

By transforming Eq. (9) from the cumulative form into an idealized definite integral form (assume pixel density to be infinity), and replacing it with a subsection integration form, the ultimate result without derivative function is shown as below:

$$\begin{aligned}\tilde{I} &\approx \frac{\int_{X_B}^{X_A} \frac{d[R(X)]}{dX} dX}{\int_{X_B}^{X_A} \frac{d[R(X)]}{dX} dX} \\ &= \frac{1}{R\,(X_A) - R\,(X_B)} \left[X_A R\,(X_A) - X_B R\,(X_B) - \int_{X_B}^{X_A} R\,(X)\,dX\right] \\ &\approx \frac{1}{R\,(X_A) - R\,(X_B)} \left[X_A R\,(X_A) - X_B R\,(X_B) - \sum_{i=A}^{B} R\,(X_i)\right]\end{aligned} \tag{10}$$

In Eq. (10), the integral interval is the pixels set from X_A to X_B, which covers the left segment of the partial-dip curve, on this segment exists the inflection. With the inflection estimate value $\tilde{I}$, the "intensity variation ratio weight" factor F_i is modified as follow:

$$\tilde{F}_i \overset{\text{def}}{=} \left|\frac{k}{\left(X_i - \tilde{I}\right)^2 \tilde{I}}\right| \tag{11}$$

Based on Eq. (10), Eq. (11) and Eq. (4), the entire twice weighted centroid algorithm is designed as Eq. (12):

$$centroid \overset{\text{def}}{=} \frac{\sum_{i=A}^{D} \tilde{F}_i \omega_i \left[R\,(X_i) - L\right] X_i}{\sum_{i=A}^{D} \tilde{F}_i \omega_i \left[R\,(X_i) - L\right]} \tag{12}$$

In next section, experimental results will demonstrate the RI resolution improvement by using the novel mechanism and the twice weighted centroid algorithm.

IV. EXPERIMENTAL VERIFICATION

In this section, the performances of the novel sensing mechanism and algorithm are tested. There are also two parts, corresponding to the results in Figure 2 and 3.

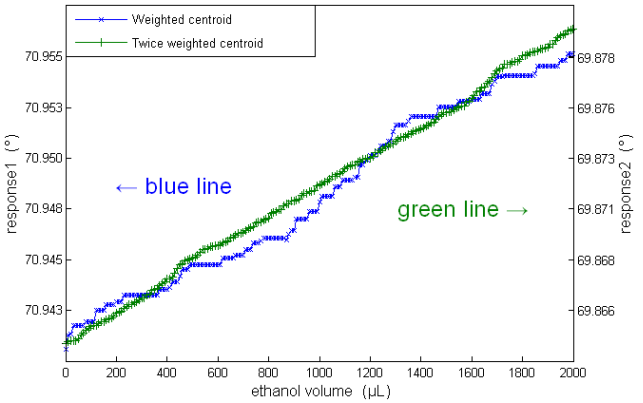

FIGURE 8. Performance comparison of continuous RI increase response evolutions. The green line indicates results calculated based on the new partial-dip observation mechanism and twice weighted centroid algorithm.

As the results of the experiment A, the SPR responses evolution corresponding to a continuous increment of ethanol volume is shown as Figure 8. For an apparent comparison, another evolution acquired under the conventional sensing mechanism is given in Figure 8. The blue line in Figure 8 has something differences with the one in Figure 2, but their main tendencies are basically same. This phenomenon demonstrates that the nonlinearity of the blue line is not occasional errors arising from noises but resulted from the sensitivity deviation [18]. From the intuitive point of view, under the novel sensing mechanism (green line), the output linearity of SPR sensor became more uniform [18], the sensitivity deviation phenomena are significantly reduced.

According to the green line in Figure 8, an approximately linear relationship is observed, which is much better for the calculation of the sensitivity parameter S. Corresponding to the injection of 2mL ethanol in 1 L water, the RI change is 0.0001RIU. Thus, sensitivity is calculated by $(69.87877 - 69.86555)/0.0001 \approx 132.2°/\text{RIU}$. In Figure 9 and Table 3, the results from the experiment B provide comparisons to Figure 2 and Table 1.

When the ethanol contents are exactly same, the responses under the partial-dip monitoring mechanism provide greatly better standard deviations. The average standard deviation

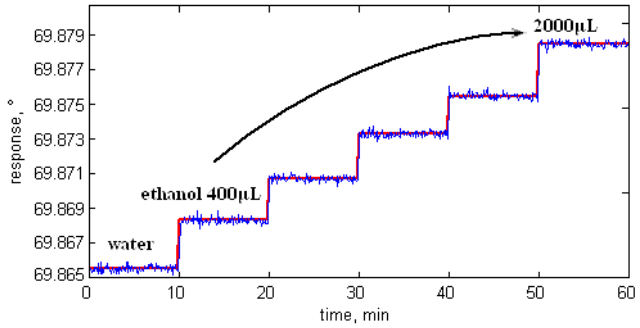

FIGURE 9. Sensor responses reproducibility characterized by ethanol samples with various RI values. The sensor responses are calculated based on the new partial-dip observation mechanism and twice weighted centroid algorithm.

TABLE 3. Statistics of responses under novel mechanism.

Ethanol content (μL)	Average of response (°)	Standard deviation of response (10^{-4} °)
0	69.86555	4.43870
400	69.86841	4.45876
800	69.87084	4.43813
1200	69.87350	4.46964
1600	69.87569	4.47871
2000	69.87877	4.46735

level of responses $\sim 4.45 \times 10^{-5}$ ° can be regarded as the improved σ_s.

By using the measured sensitivity $S \approx 132.2°/\text{RIU}$ to replace the former referent value $S \approx 120°/\text{RIU}$ [21], the RI resolution σ_{RI} under the conventional monitoring mechanism is calculated as: $\sigma_{RI} = 2.66 \times 10^{-4}/132.2 \approx 2.0 \times 10^{-6}$RIU. By using the novel sensing mechanism which uses the partial-dip and the twice weighted centroid algorithm, σ_{RI} is enhanced up to: $\sigma_{RI} = 4.45 \times 10^{-5}/132.2 \approx 3.4 \times 10^{-7}$RIU, almost approaches the temperature-dependent RI resolution limit 1.67×10^{-7}RIU.

V. CONCLUSION

In summary, a new observation mechanism is presented in this work for the identifying accuracy enhancement of spectrum-like SPR response waveforms. The analysis suggests that aiming the rapidly changing part provides a better observation target than the entire waveform for the more accurate peak locating. The experimental results of partial-dip observation illustrate that the novel mechanism is capable to lower the output standard deviation and enable better linearity. As a result, without any performance enhanced components used, the resolution of sensor output can be significantly improved nearly one order of magnitude.

ACKNOWLEDGMENT

This work made use of technical supports from the Funding Program of Tianjin Higher Education Creative Team.

REFERENCES

[1] M. Piliarik and J. Homola, "Surface plasmon resonance (SPR) sensors: Approaching their limits?" *Opt. Express*, vol. 17, no. 19, pp. 16505–16517, 2009.
[2] J. Homola, "Present and future of surface plasmon resonance biosensors," *Anal. Bioanal. Chem.*, vol. 377, no. 3, pp. 528–539, Oct. 2003.
[3] F.-C. Chien and S.-J. Chen, "A sensitivity comparison of optical biosensors based on four different surface plasmon resonance modes," *Biosensors Bioelectron.*, vol. 20, no. 3, pp. 633–642, Oct. 2004.
[4] B. Ran and S. G. Lipson, "Comparison between sensitivities of phase and intensity detection in surface plasmon resonance," *Opt. Express*, vol. 14, no. 12, pp. 5641–5650, 2006.
[5] J. Homola, I. Koudela, and S. S. Yee, "Surface plasmon resonance sensors based on diffraction gratings and prism couplers: Sensitivity comparison," *Sens. Actuators B, Chem.*, vol. 54, nos. 1–2, pp. 16–24, Jan. 1999.
[6] J. Homola, "Surface plasmon resonance sensors for detection of chemical and biological species," *Chem. Rev.*, vol. 108, no. 2, pp. 462–493, Jan. 2008.
[7] J. Homola, S. S. Yee, and G. Gauglitz, "Surface plasmon resonance sensors: Review," *Sens. Actuators B, Chem.*, vol. 54, nos. 1–2, pp. 3–15, Jan. 1999.
[8] G. Nenninger, M. Piliarik, and J. Homola, "Data analysis for optical sensors based on spectroscopy of surface plasmons," *Meas. Sci. Technol.*, vol. 13, no. 2, pp. 2038–2046, Nov. 2002.
[9] C. Thirstrup and W. Zong, "Data analysis for surface plasmon resonance sensors using dynamic baseline algorithm," *Sens. Actuators B, Chem.*, vol. 106, no. 2, pp. 796–802, May 2005.
[10] N. J. Goddard, D. Pollard-Knight, and C. H. Maule, "Real-time biomolecular interaction analysis using the resonant mirror sensor," *Analyst*, vol. 119, no. 4, pp. 583–588, Jan. 1994.
[11] K. Johansen, R. Stålberg, I. Lundström, and B. Liedberg, "Surface plasmon resonance: Instrumental resolution using photo diode arrays," *Meas. Sci. Technol.*, vol. 11, no. 11, pp. 1630–1638, Nov. 2000.
[12] S. Owega and D. Poitras, "Local similarity matching algorithm for determining SPR angle in surface plasmon resonance sensors," *Sens. Actuators B, Chem.*, vol. 123, no. 1, pp. 35–41, Apr. 2007.
[13] S. Zhan, X. Wang, and Y. Liu, "Fast centroid algorithm for determining the surface plasmon resonance angle using the fixed-boundary method," *Meas. Sci. Technol.*, vol. 22, Dec. 2011, Art. no. 025201.
[14] G. Gupta and J. Kondoh, "Tuning and sensitivity enhancement of surface plasmon resonance sensor," *Sens. Actuators B, Chem.*, vol. 122, no. 2, pp. 381–388, Mar. 2007.
[15] P. M. Boltovets and B. A. Snopok, "Measurement uncertainty in analytical studies based on surface plasmon resonance," *Talanta*, vol. 80, no. 2, pp. 466–472, Dec. 2009.
[16] B. A. Snopok and E. V. Kostyukevich, "Kinetic studies of protein–surface interactions: A two-stage model of surface-induced protein transitions in adsorbed biofilms," *Anal. Biochem.*, vol. 348, no. 2, pp. 222–231, Jan. 2006.
[17] B. H. Ong, X. Yuan, S. C. Tjin, J. Zhang, and H. M. Ng, "Optimised film thickness for maximum evanescent field enhancement of a bimetallic film surface plasmon resonance biosensor," *Sens. Actuators B, Chem.*, vol. 114, no. 2, pp. 1028–1034, Apr. 2006.
[18] T. M. Chinowsky, L. S. Jung, and S. S. Yee, "Optimal linear data analysis for surface plasmon resonance biosensors," *Sens. Actuators B, Chem.*, vol. 54, nos. 1–2, pp. 89–97, Jan. 1999.
[19] D. A. Armbruster, M. D. Tillman, and L. M. Hubbs, "Limit of detection (LQD)/limit of quantitation (LOQ): Comparison of the empirical and the statistical methods exemplified with GC-MS assays of abused drugs," *Clin. Chem.*, vol. 40, pp. 1233–1238, Jul. 1994.
[20] K. Johansen, I. Lundström, and B. Liedberg, "Sensitivity deviation: Instrumental linearity errors that influence concentration analyses and kinetic evaluation of biomolecular interactions," *Biosensors Bioelectron.*, vol. 15, nos. 9–10, pp. 503–509, 2000.
[21] C. S. Moreira, A. M. N. Lima, H. Neff, and C. Thirstrup, "Temperature-dependent sensitivity of surface plasmon resonance sensors at the gold–water interface," *Sens. Actuators B, Chem.*, vol. 134, no. 2, pp. 854–862, Sep. 2008.
[22] M. Daimon and A. Masumura, "Measurement of the refractive index of distilled water from the near-infrared region to the ultraviolet region," *Appl. Opt.*, vol. 46, pp. 3811–3820, 2007.
[23] J. P. Longtin and C.-H. Fan, "Precision laser-based concentration and refractive index measurement of liquids," *Microscale Thermophys. Eng.*, vol. 2, no. 4, pp. 261–272, Oct. 1998.

[24] R. Belda, J. V. Herraez, and O. Diez, "A study of the refractive index and surface tension synergy of the binary water/ethanol: Influence of concentration," *Phys. Chem. Liquids*, vol. 43, no. 1, pp. 91–101, Aug. 2005.
[25] E. Fujiwara, R. T. Takeishi, A. Hase, E. Ono, J. S. Santos, and C. K. Suzuki, "Real-time optical fibre sensor for hydro-alcoholic solutions," *Meas. Sci. Technol.*, vol. 21, no. 9, Jul. 2010, Art. no. 094035.
[26] K. Kurihara, K. Nakamura, and K. Suzuki, "Asymmetric SPR sensor response curve-fitting equation for the accurate determination of SPR resonance angle," *Sens. Actuators B, Chem.*, vol. 86, no. 1, pp. 49–57, Aug. 2002.
[27] K. Wang, Z. Zheng, Y. Su, Z. Wang, L. Song, and J. Zhu, "Hybrid differential interrogation method for sensitive surface plasmon resonance measurement enabled by electro-optically tunable SPR sensors," *Opt. Express*, vol. 17, no. 6, pp. 4468–4478, 2009.
[28] X. Wang *et al.*, "Shot-noise limited detection for surface plasmon sensing," *Opt. Express*, vol. 19, no. 1, pp. 107–117, Jan. 2011.

CHENG WANG received the B.E. degree in measurement and control technology from Xidian University, Xi'an, China, in 2006, the M.E. and Ph.D. degrees in communication engineering and electrical engineering from Nankai University, Tianjin, China, in 2010 and 2014, respectively.

From 2012 to 2014, the China Scholarship Council sent him to Columbia University, New York, NY, USA, as a Joint Training Doctoral Scholar. During the visiting study, he switched his research interests into condensed matter physics and nanoelectronics. After an Interdisciplinary Postdoctoral Research with Tsinghua University, Beijing, China, from 2015 to 2017, he joined Tianjin Normal University as a Principle Investigator, in 2017. His current research interest includes 2-D materials and devices.